optica

Ultraviolet-to-millimeter-band supercontinua driven by ultrashort mid-infrared laser pulses: supplementary material

A.V. Mitrofanov,[1,2,4,5] D.A. Sidorov-Biryukov,[1,2,4] M.M. Nazarov,[4] A.A. Voronin,[1,2] M.V. Rozhko,[1,2] A.D. Shutov,[2,3] S.V. Ryabchuk,[2] E.E. Serebryannikov,[1,2] A.B. Fedotov,[1,2] and A.M. Zheltikov[1,2,3,4,*]

[1] *Physics Department, International Laser Center, M.V. Lomonosov Moscow State University, Moscow 119992, Russia*
[2] *Russian Quantum Center, ul. Novaya 100, Skolkovo, Moscow Region, 143025 Russia*
[3] *Department of Physics and Astronomy, Texas A&M University, College Station TX 77843, USA*
[4] *Kurchatov Institute National Research Center, Moscow 123182, Russia*
[5] *Inst. Laser and Information Technol. - Branch of FSRC "Crystallography and Photonics," Russian Acad. Sci., Shatura, 140700 Russia*
[*] *Corresponding author: zheltikov@physics.msu.ru*

Published 3 January 2020

This document provides supplementary information to "Ultraviolet-to-millimeter-band supercontinua driven by ultrashort mid-infrared laser pulses," https://doi.org/10.1364/OPTICA.7.000015, offering an expanded description of the methods and models used in our work to analyze and understand UV-to-mm-band supercontinua driven by ultrashort, high-peak-power mid-infrared laser pulses. Technical details of the analysis of phase-matching effects in multidecade supercontinuum generation by mid-infrared laser pulses are also provided.

1. Modeling terahertz-to-millimeter-band supercontinuum generation by mid-infrared pulses

Two mechanisms may account for the generation of SC as observed in experiments. One of these mechanisms involves perturbative wave-mixing processes enabled by the nonlinear polarization and related nonlinear susceptibilities [1, 2]. In the second scenario, laser-induced tunneling leads to a rapid, almost stepwise buildup of the electron density, giving rise to a broadband optical nonlinearity [3 – 8], which shows up in a vast variety of nonlinear processes, including THz radiation [3 – 7] and harmonic generation [8]. Below, we provide details of the methods and models used in our work to analyze the nonlinear response induced by each of these two mechanisms and to understand their relation to UV-to-mm-band supercontinua observed in our experiments.

1.1. Photoionization currents

Our analysis of the photoelectron current as a source of low-frequency radiation is based on a standard semiclassical equation [1, 2, 6]

$$\partial j(\eta)/\partial\eta + \nu_e j(\eta) = (e^2/m_e)\rho(\eta)E(\eta), \qquad \text{(S1)}$$

where η is the time in the retarded frame of reference, $E(\eta)$ is the driver field, ν_e is the damping rate, e is the electron charge, and m_e is the electron mass.

The electric field radiated by the photoelectron current $j(\eta)$ is given by $E_j(\eta) \propto \partial j(\eta)/\partial\eta$. The Fourier transform of this equation leads to the spectrum of $E_j(\eta)$ in the form $E_j(\omega) \propto \omega j(\omega)$, where $j(\omega)$ is the Fourier transform of the time-dependent photocurrent $j(\eta)$,

$$j(\omega) = e^2 [m_e(\omega^2 + \nu_e^2)]^{-1}(i\omega + \nu_e)\int_{-\infty}^{\infty} \rho(\eta)E(\eta)e^{-i\omega\eta}d\eta. \qquad \text{(S2)}$$

Quantum dynamics enters into our model through the equation for the electron density, $d\rho(\eta)/d\eta = w(\eta)[\rho_0 - \rho(\eta)]$, where ρ_0 is the density of neutral species undergoing photoionization and the tunneling rate $w(\eta)$ is calculated using the quasistatic-approximation Ammosov–Delone–Krainov-type equation [1, 2, 9],

$$w(\eta)=(6/\pi)^{1/2}\omega_a|C_{n'l'}|^2 [U_0/(2Ry)] \text{ x}$$
$$\text{x } [(2E_0)/E(\eta)]^{\alpha}\exp[-(2/3)E_0/E(\eta)], \qquad \text{(S3)}$$

where $\omega_a \approx 4.13\cdot10^{16}$ Hz is the atomic unit of frequency, $E_0 = E_a(U_0/Ry)^{3/2}$, $E_a \approx 5.14\cdot10^{11}$ V/m is the atomic field, U_0 is the ionization potential, Ry is the Rydberg constant, $\alpha = 2n' - 3/2$, $|C_{n'l'}|^2 = 2^{2n'}[n'\Gamma(n' + l' + 1)\Gamma(n' - l')]^{-1}$, $n' = n - \delta l$, $l' = l - \delta l$, $\delta l = n -$

$(U_0/Ry)^{-1/2}$, $n' = n - \delta l$, $l' = l - \delta l$, $\delta l = n - (Ry/U_0)^{1/2}$, n is the principal quantum number, and l is the orbital quantum number.

1.2. Nonlinear polarization

In a perturbative, weak-field regime of nonlinear optics, a laser field $E(\eta)$ induces a third-order nonlinear polarization $P_{NL}(\eta) = \varepsilon_0\chi^{(3)}E^3(\eta)$, where $\chi^{(3)}$ is the cubic nonlinear susceptibility. The third-order nonlinear polarization $P_{NL}(\eta)$ gives rise to a variety of nonlinear signals, including a signal at the frequency of the third harmonic, $3\omega_0$, via $2\omega_0 + 2\omega_0 - \omega_0$ four-wave mixing, as well as a low-frequency, THz or sub-THz signal, sometimes referred to as an optical rectification signal, via $\omega_0 + \omega_0 - 2\omega_0$ four-wave mixing.

1.3. Parameter space

With atmospheric air at a variable pressure p chosen as a gas target, we take $\rho_0 = 5.4\cdot10^{18}(p/p_{atm})$ cm^{-3}, $U_0 = 12.1$ eV, $n = 2$, $l = 0$, and $\tau_e = 1/\nu_e = 350(p_{atm}/p)$ fs [1, 2], p_{atm} being the atmospheric pressure. The third-order susceptibility $\chi^{(3)}$ is found from the nonlinear refractive index $n_2 = 3\mu_0 c\chi^{(3)}/4n_0^2$ at 800 nm [1, 2]. Obviously, such an approach can only provide a rough approximation as it neglects the dispersion of the third-order susceptibility $\chi^{(3)}$.

The laser field is taken in the form

$$E(\eta)=E_1[\exp(-\eta^2/\tau_p^2)\cos(i\omega_0\eta)+E_2\exp(-\eta^2/\tau_p^2)\cos(2i\omega_0\eta+\theta)], \quad (S4)$$

where the fundamental-frequency and second-harmonic field amplitudes E_1 and E_2 and the pulse width τ_p are chosen in such a way as to reproduce the experimental conditions.

2. Experiment versus theory

Calculations performed with the use of the models of wave mixing and laser-driven photoelectron current as described in Section 1 above show that, in the near-IR-to-UV range, both processes yield supercontinua that exhibit $m\omega_0$ peaks with similar spectra and close intensity (cf. dashed lines and blue shading in Fig. S1a). In the THz-to-MMW part of the spectrum, however, the situation is drastically different. Here, the nonlinear signal due to wave mixing is orders of magnitude weaker than the nonlinear signal related to the photoionization current (cf. green dashed line and blue shading in Figs. S1a – S1c). The photocurrent model, on the other hand, provides fairly accurate predictions (blue shading in Fig. S1c) for the spectrum of the THz-to-MMW part of the SC observed in experiments (solid line in Fig. S1c). These findings suggest that the generation of the THz-to-MMW part of the SC in our experiments is largely due to the photoionization-current nonlinearity.

3. Effects of air refraction dispersion: mid-infrared versus near-infrared

The yield of THz radiation generated by a two-color driver consisting of a laser field at a central frequency ω and its second harmonic is sensitive to the relative phase $\Delta\varphi = \omega(n_\omega - n_{2\omega})L/c = \Delta kL/2$, where $\Delta k = (2k_\omega - k_{2\omega})$, n_ω and $n_{2\omega}$ are the refractive indices at the frequencies ω and 2ω, k_ω and $k_{2\omega}$ are the wave numbers of the fundamental-wavelength field and its second harmonic, and L is the propagation path. As the propagation path increases from 0 to $L_p = \lambda/(2\Delta n)$, with λ being the wavelength of the fundamental-wavelength field and $\Delta n = |n_\omega - n_{2\omega}|$, the relative phase grows from 0 to π, giving rise to an oscillatory behavior of the THz yield. Dispersion of the refractive index may, thus, lead to a strong dependence of the supercontinuum yield and bandwidth on the propagation path L [10 – 12].

In Fig. S2a, we present the wave-vector mismatch Δk calculated as a function of the wavelength λ for atmospheric air at a pressure of 101325 Pa, temperature of 25°C, humidity of 50%, and CO_2 concentration of 500 ppm. The refractive index of air in this analysis was calculated using the full HITRAN-database set of atomic and molecular transitions in atmospheric air [13]. With the driver wavelength λ set at a typical wavelength of a Ti: sapphire laser, λ = 800 nm, the wave-vector mismatch $|\Delta k|$ for atmospheric air is seen to be as large as $|\Delta k| \approx 120$ m^{-1}, leading to L_p of a few centimeters, in agreement with experiments [10, 11, 14]

In the mid-infrared range, however, dispersion of the refractive index of air is much weaker [15]. Specifically, with the driver wavelength λ set at a typical wavelength of a mid-infrared OPCPA output used in our experiments, $\lambda_0 = 3.9$ μm, we find $|\Delta k| \approx 1.5$ m^{-1} (Fig. S2a), which is nearly two orders of magnitude smaller than typical $|\Delta k|$ values in a near-infrared experiment. The corresponding L_p values fall in the range of several meters and are much larger than the propagation paths in our experiments.

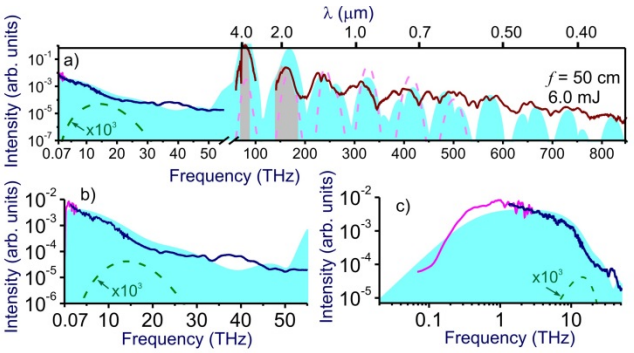

Fig. S1. (a) The spectrum of the MMW-to-UV supercontinuum: (solid line) mid-IR-to-UV (wine line) and THz-to-MMW (blue and pink lines) parts of the SC spectrum measured in experiments in atmospheric air with a two-color laser driver with $\lambda_0 \approx 3.9$ μm, $\tau_0 \approx 80$ fs, $E_0 \approx 6.0$ mJ, $f \approx$ 50 cm, (blue shading) calculations using the photoionization current model, (green and pink dashed line) calculations using the nonlinear polarization model in the mid-IR-to-UV (pink dashed line) and THz-to-MMW (green dashed line, note a 10^3 multiplier). The abscissa scale changes from linear to logarithmic at 55 THz. (c, d) The spectrum of the THz–MMW part of the supercontinuum: (solid line) Fourier transform of the EOS (pink line) and autocorrelation (blue line) experimental traces, (blue shading) calculations using the photoionization current model, (green dashed line) calculations using the nonlinear polarization model (note a 10^3 multiplier).

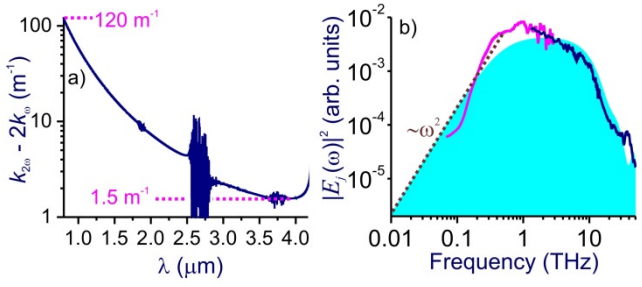

Fig. S2. (a) The wave-vector mismatch for $\omega_0 + \omega_0 - 2\omega_0$ four-wave mixing in atmospheric air as a function of the wavelength of the ω_0 driver. (b) The MMW-to-THz part of the SC spectrum: (solid line) Fourier transform of the EOS (pink line) and autocorrelation (blue line) experimental traces, (blue shading) calculations using the photoionization current model, (dotted line) the ω^2 asymptote.

4. The $\omega \rightarrow 0$ limit: no propagation for the dc field

The photocurrent model used in our analysis does not include any propagation effects. However, the radiation source term in this model, $\partial j(\eta)/\partial\eta$, is overall consistent with a canonical picture of diffraction in the far field, as diffraction-integral analysis leads to a source term of the $\partial j(\eta)/\partial\eta$ form in the far field [15]. Thus, even though the model used in our analysis does not include propagation effects, it helps reproduce important signatures of far-field diffraction. Indeed, the Fourier transform of the field radiated by $j(\eta)$, $E_j(\eta) \propto \partial j(\eta)/\partial\eta$, leads to an intensity spectrum $|E_j(\omega)|^2 \propto |\omega j(\omega)|^2$ with a signature ω^2 factor, typical of far-field radiation spectra [16]. That $|E_j(\omega)|^2$ decreases toward lower frequencies and vanishes at $\omega = 0$ is consistent with dc-field no-propagation – another signature result of diffraction theory. It is pleasing that the low-frequency wing of the experimental SC spectra (pink line in Figs. S2b) agrees well with predictions of the photocurrent model (blue shading in Figs. 2c, 2f). In particular, at very low ω, experimental spectra closely follow the ω^2 scaling (dotted line in Fig. S2b, in full agreement with diffraction theory.

5. Effective size of the MMW–THz radiation source

The photoelectron current $j(\eta)$ is initially induced by a laser driver within the laser beam-waist region. The low-frequency part of its radiation spectrum, however, is emitted within time intervals much longer than the driver pulse width. Specifically, the low-frequency cutoff ν_{off} in the spectrum of the field $E_j(\eta) \propto \partial j(\eta)/\partial\eta$ radiated by the photoelectron current $j(\eta)$ is defined by a typical decay time τ_e of $j(\eta) \propto \exp(-\eta/\tau_e)$, which is in many cases related to a generic collision process [6]. Since photoelectrons continue to move within this time interval, the spatial extent d_s of the photocurrent source of the MMW–THz radiation field may considerably differ from the beam-waist size of the driver field. As the amplitude of a generic electron quiver motion increases with the driver wavelength λ_0, one can expect that the size d_s of the MMW–THz radiation source should rapidly increase with λ_0.

The navy line in Fig. S3a shows a two-color driver field $E(\eta)$ with parameters typical of our experiments. The photoionization rate $w(\eta)$ calculated for such a field using Eq. (S3) is shown by blue shading in Fig. S3a. The trajectories of photoelectrons generated by the driver field depend on the instant of time at which these photoelectrons are born via photoionization. Some electrons oscillate back and forth within the beam-waist regions. Others pick up the momentum and move outside the beam-waist area. The pink line in Figs S3a and S3b shows the displacement x calculated for one of such departing photoelectrons. This displacement is found by solving the relevant classical equations of motion for a photoelectron whose birth time η_0 (shown by the dotted line in Fig. S3a) is chosen in such a way as to allow the electron to catch the phase of the laser field that drives electrons outside the beam-waist region, giving rise to large x-displacements of photoelectrons in the wake of the driver pulse. The displacement x_m that photoelectrons moving along such a trajectory reach within the time interval τ_e. ~ 1 ps can be as large as a few millimeters. Specifically, for the photoelectron trajectory shown in Figs. S3a and S3b, $x_m \approx 4$ mm. This is, of course, an extreme case of possible photoelectron trajectories. For most of the photoelectrons, x_m displacements are smaller, with $x_m \approx 4$ mm providing an upper-bound estimate for the size d_s of the photocurrent source of MMW–THz radiation. It is remarkable, however, that this upper-bound estimate is consistent with a typical low-frequency cutoff, $\lambda_{off} \sim 3 - 4$ mm, in SC spectra observed in our experiments (Figs. 2f, S2b).

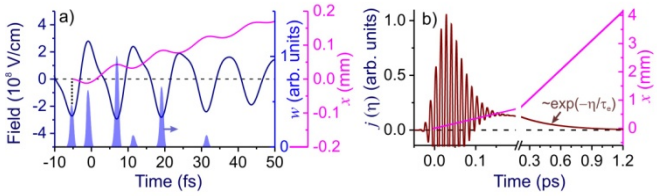

Fig. S3. A two-color driver field (navy line), photoionization rate (blue shading), photoelectron current $j(\eta)$ (maroon line), and the transverse displacement of a photoelectron on an extreme departing trajectory (pink line) on a fine (a) and coarse (b) time scale. The instant of time at which the photoelectron is produced via photoionization is shown by the vertical dotted line.

6. Effects of collisions

In this section, we focus on the effects of collisions in photocurrent radiation. Collisions are included in the photocurrent model as a separate term in the equation for the dynamics of the photoelectron current [Eq. (S1)], translating into a ν_e-dependent term in the equation for the spectrum of the photocurrent [Eq. (S2)]. As one important tendency, collisions damp the photocurrent dynamics driven by the laser field, defining, along with the duration of photoionization steps in $j(\eta)$, the low-frequency cutoff in photocurrent radiation spectra. However, the asymptotic behavior of photocurrent radiation spectra $j(\omega)$ at very low frequencies, below this low-frequency cutoff, follows the ω^2 scaling regardless of the collision rate and even regardless of the model of the current or the model of collisions.

These arguments are illustrated by calculations presented in Fig. S4, which displays the long-wavelength part of the power spectra $|E_j(\omega)|^2$ of radiation generated by a two-color laser field (S4) in atmospheric air with a pressure p varying from 1 to 800 mbar. As expected, the $|E_j(\omega)|^2$ spectra in Fig. S4 are seen to exhibit a well-defined long-wavelength cutoff, which shifts toward longer wavelengths at lower p. This behavior of the long-wavelength cutoff is readily understood in terms of the collision rate ν_e, which is proportional to p. The low-frequency asymptotic behavior of $|E_j(\omega)|^2$ beyond this cutoff is seen to follow the ω^2 scaling (shown by the dotted line in Fig. S4), which is typical of far-field radiation spectra in a broad class of diffraction settings [16].

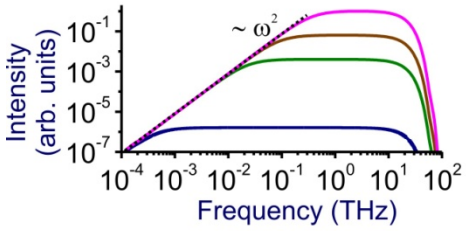

Fig. S4. The long-wavelength part of the power spectra $|E_j(\omega)|^2$ of radiation generated by a two-color laser field (S4) in atmospheric air with a pressure p = 1 mbar (blue line), 50 mbar (green line), 200 mbar (brown line), and 800 mbar (pink line). The ω^2 asymptote is shown by the dotted line.

References

1. L. Bergé, S. Skupin, R. Nuter, J. Kasparian, and J.-P. Wolf, "Ultrashort filaments of light in weakly ionized, optically transparent media," Rep. Prog. Phys. **70**, 1633-1713 (2007).

2. A. Couairon and A. Mysyrowicz, "Femtosecond filamentation in transparent media," Phys. Rep. **441**, 47 – 189 (2007).
3. K. Y. Kim, A. J. Taylor, J. H. Glownia, and G. Rodriguez, "Coherent control of terahertz supercontinuum generation in ultrafast laser-gas interactions," Nature Photonics **2**, 605–609 (2008).
4. M. D. Thomson, V. Blank, and H.G. Roskos, "Terahertz white-light pulses from an air plasma photo-induced by incommensurate two-color optical fields," Opt. Express **18,** 23173-23182 (2010).
5. M. Clerici, M. Peccianti, B. Schmidt, L. Caspani, M. Shalaby, M. Giguère, A. Lotti, A. Couairon, F. Légaré, T. Ozaki, D. Faccio, and R. Morandotti, "Wavelength Scaling of Terahertz Generation by Gas Ionization," Phys. Rev. Lett. **110,** 253901 (2013).
6. I. Babushkin, S. Skupin, A. Husakou, C. Köhler, E. Cabrera-Granado, L. Bergé and J. Herrmann, " Tailoring terahertz radiation by controlling tunnel photoionization events in gases," New J. Phys. 13, 123029 (2011).
7. A. Nguyen, K. J. Kaltenecker, J.-C. Delagnes, B. Zhou, E. Cormier, N. Fedorov, R. Bouillaud, D. Descamps, I. Thiele, S. Skupin, P. U. Jepsen, and L. Bergé, "Wavelength scaling of terahertz pulse energies delivered by two-color air plasmas," Opt. Lett. **44,** 1488-1491 (2019).
8. A.V. Mitrofanov, A.J. Verhoef, E.E. Serebryannikov, J. Lumeau, L. Glebov, A.M. Zheltikov, and A. Baltuška, "Optical detection of sub-cycle ionization dynamics in transparent dielectrics," Phys. Rev. Lett. **106**, 147401 (2011).
9. M.V. Ammosov, N.B. Delone, V.P. Krainov, " Tunnel ionization of complex atoms and of atomic ions in an alternating electromagnetic field," JETP 64, 1191 (1986).
10. K. Y. Kim, J. H. Glownia, A. J. Taylor and G. Rodriguez, "Terahertz emission from ultrafast ionizing air in symmetry-broken laser fields," Opt. Express 15, 4577-4584 (2007).
11. M. Kress, T. Löffler, S. Eden, M. Thomson, and H.G. Roskos, "Terahertz-pulse generation by photoionization of air with laser pulses composed of both fundamental and second-harmonic waves," Opt. Lett. 29, 1120-1122 (2004).
12. M. D. Thomson, M. Kreβ, T. Lëoffler, and H.G. Roskos, "Broadband THz emission from gas plasmas induced by femtosecond optical pulses: From fundamentals to applications," Laser & Photon. Rev. **1**, 349-368 (2007).
13. URL: www.cfa.harvard.edu/hitran/
14. D. Kartashov, S. Ališauskas, A. Pugžlys, A. A. Voronin, A. M. Zheltikov, and A. Baltuška, "Third- and fifth-harmonic generation by mid-infrared ultrashort pulses: beyond the fifth-order nonlinearity," Opt. Lett. **37,** 2268-2270 (2012).
15. O.D. Jefimenko, *Electricity and Magnetism* (Appleton, New York, 1966).
16. S.A. Akhmanov and S.Yu. Nikitin, *Physical Optics* (Clarendon, Oxford, 1997).